AERODYNAMIC RESULTS FROM THE STAR HOVER TEST: AN EXAMINATION OF ACTIVE TWIST ACTUATION

A. Bauknecht*, B. Ewers*, O. Schneider**, M. Raffel*

Abstract

Active rotor control concepts, such as active twist actuation, have the potential to effectively reduce the noise and vibrations of helicopter rotors. Within the STAR (Smart Twisting Active Rotor) hover test, an active twist rotor was tested in the rotor preparation hall at DLR Braunschweig. The rotor blades were actuated with frequencies of $1/rev - 5/rev$ and peak torsion amplitudes of up to $2°$. This paper describes aerodynamic results from the hover test based on time-resolved stereoscopic PIV measurements at the forward blade tip position. Continuous time series of flow fields behind the blade tips were evaluated to investigate the young blade tip vortices between $\psi_v = 3.56°$ and $45.74°$ of vortex age. For the unactuated baseline case, the vortex trajectory, blade tip scattering, and temporal development of the peak axial and swirl velocity are discussed. The effects of the active twist actuation on the blade tip vortices are examined for the $1/rev$ and $3/rev$ actuation frequencies. The variation of the vortex trajectories is dominated by the blade tip deflection for the $1/rev$ actuation, and by the torsion of the blade tip for the $3/rev$ actuation. The $3/rev$ actuation reduces the initial peak swirl velocity by up to 35% compared to the baseline case. The actuation with the control phase angles $\varphi_3 = 45° - 135°$ achieves a strong variation of the vortex trajectories with a vertical deviation of up to $2.6\%R$ below the rotor tip path plane. The present aerodynamic investigation reveals a high control authority of the actuators – especially for the $3/rev$ actuation frequency – on the vortex trajectories and the vortex strength, thus demonstrating the usefulness of the active twist concept.

NOMENCLATURE

a	Velocity fit parameter
c	Blade chord length, m
C_T	Thrust coefficient, $C_T = T/(\rho\pi\Omega^2R^4)$
k	Control frequency
L_m	Measurement resolution, m
M_t	Tip Mach number
n	Vatistas swirl shape parameter
N_b	Number of blades
r	Radial coordinate, m
r_c	Vortex core radius, m
R	Rotor radius, m
t	Time, s
T	Rotor thrust, N
u, v, w	Velocity components, m/s
U_n	Maximum control amplitude, V
U_i	Control voltage signal, V
V_{tip}	Blade tip speed, $V_{tip} = \Omega R$, m/s
V_z	Vortex induced axial velocity, m/s
V_θ	Vortex induced swirl velocity, m/s
x, y, z	Coordinates in PIV image plane, m
α_{tip}	Blade tip angle, deg
Γ_v	Vortex circulation, m^2/s
λ_2, Q	Flow field operators, $1/s^2$
λ, λ_{ci}	(Signed) swirling strength, $1/s$
λ_i	Non-dimensional rotor inflow velocity
ρ	Air density, kg/m^3
σ	Rotor solidity, $\sigma = N_bc/(\pi R)$
φ	Control phase, rad
ψ_v	Vortex age, deg
Ψ	Azimuth, $\Psi = \Omega t$, deg
ω_z	Vorticity normal to x-y plane, $1/s$
Ω	Rotor rotational frequency, rad/s

1 INTRODUCTION

Active rotor control concepts such as HHC [19, 20] (Higher Harmonic Control), active trailing edge (TE) flaps [17], and active twist blades [26] have the potential to effectively reduce the noise and vibrations of helicopter rotors caused by blade-vortex interactions (BVI). In the STAR (Smart Twisting Active Rotor) hover test, an active twist rotor based on the design of the 41% Mach-scaled Bo 105 blades was tested in the rotor preparation hall at DLR Braunschweig. The test comprised measurements of the rotor forces and moments, optical and on-blade acquisition of the blade angle and deformation, on-blade pressure measurements, and a characterization of young blade tip vortices via high-speed stereoscopic Particle Image Velocimetry (PIV) and the high-speed Background-Oriented Schlieren (BOS) technique. An overview of the measurement program including representative results and a preliminary PIV evaluation was given by

*German Aerospace Center (DLR), Institute of Aerodynamics and Flow Technology, Bunsenstr. 10, 37073 Göttingen, Germany, Andre.Bauknecht@dlr.de

**German Aerospace Center (DLR), Institute of Flight Systems, German Aerospace Center (DLR), Lilienthalplatz 7, 38108 Braunschweig, Germany

Hoffmann et al. [7]. In the present paper, these preliminary PIV results are complemented by a thorough and detailed analysis of the PIV data corresponding to an unactuated test case, a thrust variation study, and a series of active twist actuation cases. The temporal resolution of the PIV recordings allowed for the analysis of time-resolved vortex trajectories. Characteristic vortex properties such as the maximum axial V_z and swirl velocity V_θ were computed based on individual velocity fields and consequently phase averaged (see *individual averaging*, [12]). With the results of the PIV measurements, an investigation of the effects of the active twist actuation on the blade tip vortex system of the STAR rotor under hover condition was performed.

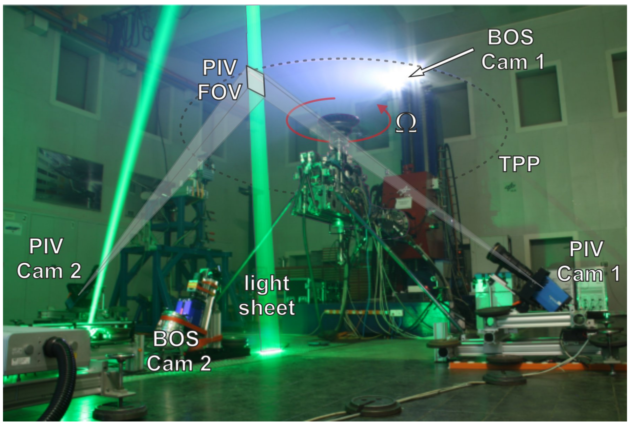

Figure 1: STAR hover test setup. The positions of the PIV and BOS cameras, the PIV field of view (FOV), and the tip path plane (TPP) are marked

2 EXPERIMENTAL SETUP

In 2013, an aerodynamic hover test of the STAR active twist rotor blades was conducted in the rotor test chamber at DLR Braunschweig. The STAR rotor blades were designed based on a 41% Mach-scaled geometry of the BO 105 rotor blades, resulting in a radius of $R = 2$ m and a chord length of $c = 0.121$ m. The blades for the fully articulated rotor without a pre-cone were designed for a clockwise sense of rotation with a linear pre-twist of $-8°/R$ starting at a radius of $r = 0.44$ m. Due to manufacturing complications, the real pre-twist varied from blade to blade between $-10.3°/R$ and $-11.3°/R$. Piezoceramic MFC (Macro Fiber Composite) actuators [16] were integrated into the upper and lower blade skin to generate the active blade twist. Details on the manufacturing, build-up, and previous testing of the STAR rotor blades are given in [25, 6, 7].

2.1 Test rig

The hover test of the STAR program was conducted on the DLR rotor test rig ROTEST II [3] inside a test chamber of $12\,\text{m} \times 12\,\text{m} \times 8\,\text{m}$ size, as shown in Fig. 1. The ROTEST II test rig consists of a six-component rotor balance, a swash plate actuation system, and a main rotor drive system powered by a 160 kW hydraulic motor. Blade angle measurements were performed at a radial position of $r = 0.0375\,R$ by potentiometers at the lead-lag and flap hinges and at the blade attachment for pitch. Two slip rings were installed on the test rig: a conventional slip ring for the power supply and signal transmission for all blade sensors, and a high-voltage slip ring for the transmission of high-voltage control signals for the MFC actuators. All rotor data was recorded by a Transputer-based TEDAS II computer at a sampling rate of $128/rev$ (2.22 kHz). Data acquisition was synchronized with the rotor rotation by an azimuth encoder on the rotor shaft and triggered by a $1/rev$ reference signal.

The test rig with the STAR rotor was centered in the rotor preparation hall and placed at a hub height of $1.38\,R$ above the ground without inclination of the rotor tip path plane.

Figure 2: STAR active twist rotor blades with MFC actuators

Consequently, the rotor was operated in moderate ground effect and recirculation, and the rotor speed was a nominal $1041\,rpm$ ($\Omega = 109$ rad/s), corresponding to a tip Mach number of $M_t = 0.63$. The anticipated nominal rotor thrust for the STAR wind tunnel test phase was $T = 3581$ N. Due to increasing unsteadiness of the flow and the rotor dynamics with increasing thrust, this value had to be reduced to a nominal thrust of $T = 2450$ N for the hover test, corresponding to a thrust coefficient of $C_T = T/(\rho\pi\Omega^2R^4) = 0.0035$ and a blade loading of $C_T/\sigma = 0.045$, where $\sigma = N_b c/(\pi R)$ is the rotor solidity and N_b is the number of blades. The reduced thrust level allowed for a meaningful analysis of the impact of active twist actuation on the blade tip motion, and the trajectories and properties of the blade tip vortices.

A picture of the STAR rotor blades is shown in Fig. 2. The blades were equipped with 14 strain gages to measure the flap-bending, lead lag, and torsion moments, 24 strain gages for measuring the blade deformation and 186 pressure transducers integrated into the rotor blades. The majority of the sensors were distributed on blades 1 and 3, whereas blades 2 and 4 had less sensors and multiple dummy sensors instead for compensating the corresponding structural and dynamical differences. According to Riemenschneider [15], this measure did not fully succeed in harmonizing all blades. Therefore, the blades 1 and 3 with a similar blade stiffness and axis position were assembled on opposite sides of the rotor, as were the similar blades 2 and 4.

In addition to the data acquisition on the test rig and the instrumented blades, two optical systems measured the blade deformation independently. A camera system acquired the blade tip deformation at an azimuthal position of $\Psi = 270°$ by tracking two LEDs (Light Emitting Diodes) embedded in the blade tips. In a second test after the PIV and BOS measurements, a dual camera SPR (Stereo Pattern Recognition) system measured the blade deformation along the span at the $\Psi = 180°$ position. A detailed description of both systems is given in [7].

The two optical deformation measurement systems as well as the PIV and BOS systems acquired data at certain states of blade motion. In order to investigate a complete cycle of the blade motion, the phase of the active twist control signal was changed in increments of $45°$, while keeping the azimuthal positions of the optical measurement systems constant. This approach was less time-consuming than the azimuthal traversing of all measurement systems and assumed to be a good compromise between a high azimuthal measurement resolution and the number of configurations that could be tested in the scope of the test.

2.2 Active twist actuation

Each blade featured 12 piezoceramic MFC actuators that were integrated into the upper and lower blade skin. The actuators worked in a fiber direction of $\pm 45°$ with respect to the longitudinal blade axis and depending on upper and lower side. The maximum voltage range of the actuators (-500 V to $+1500$ V) had to be restricted to a maximum of $+600$ V to prevent short circuits within the actuators. These short circuits were caused by cracks in the piezoceramics of the MFC actuators that increased in number with operational time. This problem had not occurred for the previous active twist blades and was counteracted by restricting the maximum control voltage and repairing short-circuited actuators. Despite these measures, the actuator performance diminished over time and it was therefore decided that wind tunnel entry was not reasonable for the project.

The high supply voltage required by the actuators was generated by three Trek PZD2000A amplifiers per blade. The MFC actuators were controlled by a Matlab/Simulink-code running on a real time dSPACE system. The control signal was triggered by the $1/rev$ reference signal and simultaneously applied to the actuators in all four blades, so that each blade experienced the same control law at the same rotor azimuth. The actuators on the lower and upper skin were controlled in phase and with a phase-shifted cosine signal for the excitation of higher-harmonic blade torsion oscillation. With a maximum control amplitude of $U_n = 600$ V and no voltage offset, the control voltage signal $U_i(\psi)$ over the rotor azimuth ψ was defined for the i-th blade by Eq. 1 [7]:

$$U_i(\psi) = U_{k,i}(\psi) \cdot \cos(k\psi - \varphi_i - \varphi_k) \quad (1)$$
$$\text{with} \quad \varphi_i = (i-1) \cdot 90°$$

where φ_k is the control phase and k the control frequency as a multiple integer of the rotational frequency, reaching values of 0 to 5. Positive voltage amplitude corresponds to a nose-down moment.

Apart from the active twist test cases, the test program for the hover experiment included unactuated rotor measurements of the Figure of Merit with a thrust variation of $500 - 3581$ N and measurements of the fan diagram with blade speeds of $30\% - 100\%$ nominal blade speed.

2.3 High-speed PIV setup

Stereoscopic high-speed PIV and high-speed BOS measurements were conducted during the STAR hover test. Both measurement systems were focused on the near-field flow domain behind the rotor blade tip containing the blade tip vortex. The PIV and BOS measurements were conducted at a rotor azimuth of $\Psi = 180°$ as the flow field was assumed to be rotationally symmetrical, and the optical access was best at the forward blade position. The BOS system consisted of two PCO Dimax cameras located on the floor in front of the $\Psi = 180°$ position of the rotor, and on top of the $\Psi = 0°$ position, as well as two corresponding retro-reflective background screens that were illuminated by high-power pulsed LED spots close to the cameras. Comparable BOS measurements of the blade tip vortices of a helicopter model in forward flight were also described by Heineck et al.[5]. In the present paper, only the evaluation and analysis of the PIV data set will be addressed.

The stereoscopic high-speed PIV system also consisted of two PCO Dimax cameras as well as a high-speed laser. The cameras were equipped with lenses with a focal length of 300 mm and rigidly mounted in a Scheimpflug configuration at a height of 0.6 m above the ground with an angle of $90°$ between the cameras. The vertical measurement region was located at a radial position between $0.96\,R$ and $1.01\,R$ at the forward blade position $\Psi = 180°$ with an overall size of about 94 mm $\times$ 83 mm and a resolution of 1152×820 pixels. This corresponds to a measurement resolution of 12.2 pixel/mm in radial and 9.9 pixel/mm in vertical direction. A two-sided, two-level calibration target was placed within the field of view of both cameras at the position of the light sheet to calibrate the PIV cameras prior to each test sequence. The height, azimuthal, and radial position of the target were measured and kept constant throughout the measurement campaign.

A Litron LDY 300 Nd:YLF high-speed laser with two separate cavities was used as a light source. The two sequentially generated laser pulses have a temporal length of 5 ns and a frequency-dependent pulse energy of $20 - 30$ mJ. A cylindrical lens optic was used to generate a light sheet with a thickness of approximately 2.5 mm and a length of approximately 300 mm within the measurement region. Two mirrors behind the optics and above the rotor were used to align the light sheet with the measurement location at the $\Psi = 180°$

position of the rotor plane, ensuring increased particle visibility by forward scattering and a close to perpendicular intersection of the tip vortices. For the measurements, the entire rotor preparation hall including the measurement region was densely seeded with an aerosol of Di-Ethyl-Hexyl-Sebacate (DEHS) droplets of $0.26\mu m$ mean diameter[1]. The particle images were recorded using the commercial PIV software Davis 8.1.4. For a single measurement point, $10-20$ full revolutions of the rotor were captured with 124 images per revolution and continuous vortex sequences of up to 20 images. The size of the combined field of view of the two cameras enabled the study of the creation and convection of young vortices between vortex ages of $\psi_v = 3.56°$ and $\psi_v = 45.74°$, as measured from the passage of the quarter chord line. Phase-locked image acquisition was triggered with an integer fraction of the rotor encoder signal at a rate of $128/rev$ ($\Delta\Psi = 2.8125°$) or 2.22 kHz. A time delay of $29.4\mu s$ was chosen between the two image acquisitions, corresponding to a blade rotation of $\Delta\Psi = 0.18°$.

3 DATA PROCESSING

The commercial PIV software Davis 8.2.0 was used for the evaluation of the recorded particle images, as shown in Fig. 3. In an initial step, the particle images – as shown in Fig. 3a – of both cameras were evaluated with a multi-grid stereoscopic cross-correlation algorithm, starting at interrogation windows of 96×96 pixels and refined down to adaptive interrogation windows of 16×16 pixels with a window overlap of 75%. Fig. 3b depicts a typical velocity field at nominal conditions and a vortex age of $\psi_v = 28.87°$. The graph features a contour plot of the out-of-plane velocity component w and every fourth vector of the in-plane velocities u, v. The quantitative analysis of the vortex parameters was based on these highly resolved and unfiltered, two-dimensional, three-component (*2D3C*) vector fields. In a second step, the fine vector fields were post-processed with Gaussian smoothing and a median filter, and interpolated onto a coarse grid corresponding to an interrogation window size of 32×32 pixels with an overlap of 50%. The coarse vector field served as a basis for the vortex center detection, which was adapted from the algorithms described by van der Wall & Richard [21]. In addition, mapped particle images were exported for the automatic detection of particle voids (shown in Fig. 3a) and blade tips. Within the following section, the vortex localization and analysis methods are described in detail.

3.1 Vortex detection

Rotor blade tip vortex centers are typically identified based on flow field operators that take on extreme values in the vortex core due to the large local flow gradients. Common

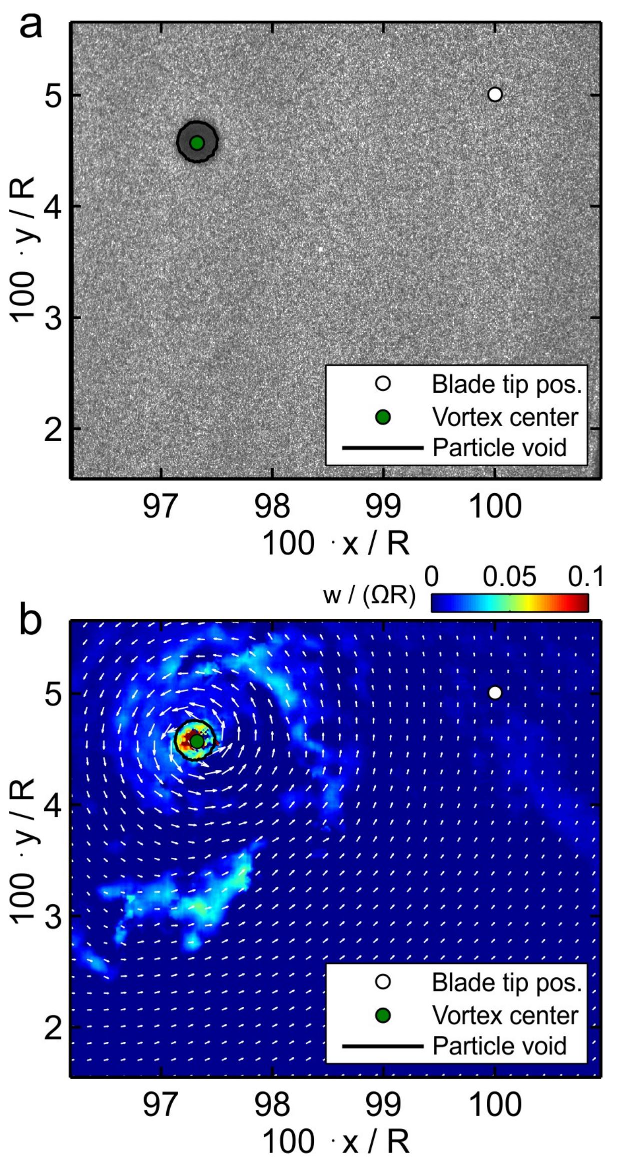

Figure 3: **a)** Particle image and **b)** velocity field at nominal conditions and $\psi_v = 28.87°$ with vortex center, void outline, and blade tip TE position

operators include the vorticity normal to the image plane ω_z, the eigenvalues of the velocity gradient tensor λ_2, the swirling strength λ_{ci}^2 (discriminant of the characteristic equation Q,[27]), and variations thereof [8, 1, 21, 18]. Following the derivations described in these papers for in-plane coordinates x, y, an out-of-plane coordinate z, and the corresponding velocities u, v, w, the following operators and definitions were used in the present study:

$$\omega_z = \left(\frac{\partial v}{\partial x} - \frac{\partial u}{\partial y}\right) \tag{2}$$

$$\lambda_2 = \frac{\left(\frac{\partial u}{\partial x}\right)^2 + \left(\frac{\partial v}{\partial y}\right)^2}{2} + \frac{\partial v}{\partial x}\frac{\partial u}{\partial y} \tag{3}$$

$$Q = \frac{\left(\frac{\partial u}{\partial x} + \frac{\partial v}{\partial y}\right)^2}{4} + \frac{\partial v}{\partial x}\frac{\partial u}{\partial y} - \frac{\partial u}{\partial x}\frac{\partial v}{\partial y} \tag{4}$$

[1] Average diameter according to the probability density function (PDF) of the distribution of length: $0.26\mu m$. Average diameter according to the PDF of the distribution of volume (accounts for visibility): $0.77\mu m$.

$$(5)\quad \lambda_{ci} = max\left(\Im(\frac{\frac{\partial u}{\partial x}+\frac{\partial v}{\partial y}}{2}+\sqrt{Q}),\Im(\frac{\frac{\partial u}{\partial x}+\frac{\partial v}{\partial y}}{2}-\sqrt{Q})\right)$$

$$(6)\quad \lambda = \lambda_{ci}\cdot\frac{\omega_z}{|\omega_z|}$$

where λ_{ci} is the swirling strength with the imaginary parts $\Im$ of the eigenvalues of Q, and λ is the signed swirling strength $\lambda_{ci}\cdot\frac{\omega_z}{|\omega_z|}$, which includes the sense of rotation of the vortices [18].

The vortices generated by adequately loaded rotor blades under hover conditions are well defined and can be localized by identifying the peak value of any of the operators described in Eq. 2-6. The vortex detection by a global peak search of a suitable flow field operator, however, proved to be unstable, especially for very young vortices and vortices generated by heavily actuated blades, as sometimes more than one peak was present in the data set, see e.g. Fig. 4b. The vortex localization was improved by applying a norm shape function convolution filter to the smoothed and coarse vector grid, as described by van der Wall & Richard [21]. Fig. 4a shows the 2D Gaussian-distributed curve f used as a norm shape function for the vorticity and swirling strength filtering. The parameters of f were adapted to fit the expected vortex core radius and the peak value of the flow field operator at the vortex center position. By calculating the convolution of the vorticity field with the adapted norm shape function, the peak corresponding to the location of the blade tip vortex is preserved, while secondary peaks, e.g. due to the vortex sheet behind the blade, are suppressed, see Fig. 4c. The exact position of the vortex center was determined by computing the area center around the maximum value of the filtered operator, based on values above a threshold of 80% of the peak value. A detail of the filtered vorticity field of Fig. 4c is plotted in Fig. 4d. It shows the vortex center positions detected by the convolution-filtered area center of the vorticity field (x_c, y_c) and the other flow field operators specified in Eq. 3-6. For a few measurement images, the vortex detection with the area center of the convolution-filtered vorticity operator produced unphysical results. In these cases, the vortex position found by one of the other operators was selected instead.

The above described vortex detection routine was applied to continuous image series starting at each blade passage. The found vortex positions were combined into vortex trajectories. Fifth order polynomial curves were fitted to these trajectories and analytically derived to compute the vortex convection velocity for each measurement image. The convection velocities were then applied for the correction of the fine velocity fields, which were used for the detailed analysis of the vortex parameters.

3.2 Swirl velocity

In a second part of the evaluation, the finer velocity fields created by the cross-correlation evaluation with the

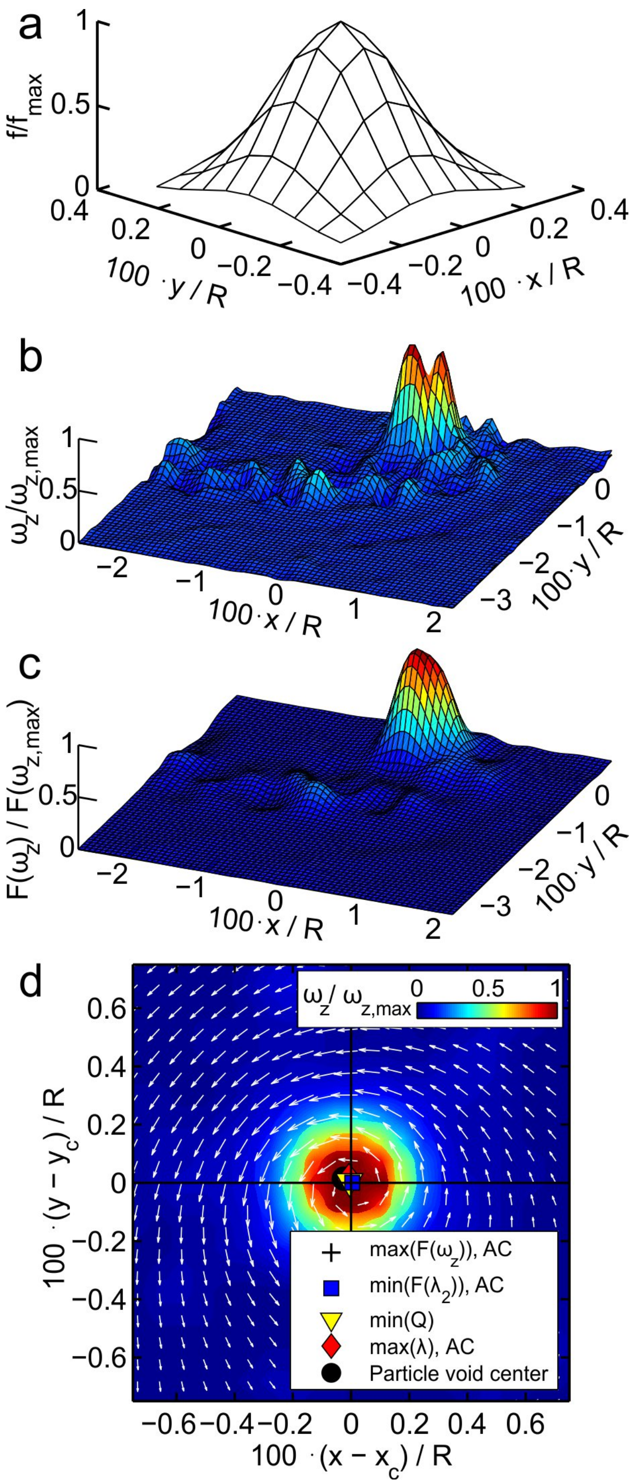

Figure 4: **a)** norm shape function for the convolution filter, **b)** unfiltered vorticity field, **c)** convolution-filtered vorticity field, **d)** detail of the vorticity field with detected center positions

16×16 pixel interrogation windows were processed to determine vortex parameters such as the core radius r_c and the swirl velocity V_θ around the vortex core. In a first step, the instantaneous convection velocity of the vortex – as determined from the vortex trajectories – was subtracted from the raw velocity fields to transform them into the vortex coordinate system. The velocity vectors within a radius of

$r = 0.2c$ around the vortex center were interpolated onto a polar grid of comparable grid size and decomposed into radial and azimuthal (V_θ) components. A typical swirl velocity distribution is shown in Fig. 5 for a vortex age of $\psi_v = 28.87°$. The blue dots represent the average of the individual radial cuts through the vortex center with unfilled points marking masked out velocities within the particle void. The standard deviation of the radial cuts is shown as a light blue area around the average data points and a spline fit through the valid average points is plotted as a solid line. The graph shows that the particle void influences the detection of the maximum swirl velocity and core radius. It also demonstrates that a simple average of the azimuthal profiles underestimates the peak swirl velocities. Therefore, the individual radial $V_\theta(r)$ profiles for each azimuthal cut through the vortex were sorted by their peak velocity and the median of the highest 10% of the curves was computed to obtain a high level swirl velocity profile. This calculation was chosen to derive a stable measure for the highest swirl velocities, which strongly contribute to the generation of noise during a blade-vortex interaction. The Vatistas vortex model [23] was fitted to the high level swirl velocity profile. The model is given in Eq. 7:

(7) $$V_\theta = \frac{\Gamma_v}{2\pi}\left[\frac{r}{(r_c^{2n} + r^{2n})^{1/n}}\right],$$

where Γ_v is the circulation of the vortex at large distances, r is the radial distance from the vortex center, and n is an integer parameter. For a value of $n = 1$ the Vatistas model corresponds to the Kaufmann or Scully vortex model, $n \to \infty$ gives the model of the Rankine vortex, and for $n = 2$, the formulation becomes a close approximation of the Lamb-Oseen model. For the curve fit in the present study, a value of $n = 2$ was chosen, which Bhagwat & Leishman [2] found to be a good match for rotor blade tip vortices. The vortex core radius r_c was determined as the radial position of the maximum swirl velocity V_θ of the Vatistas model fit to the high level swirl velocity profile.

3.3 Measurement accuracy and averaging

The vortex detection carried out in this study was based on the velocity field within and around the vortex core. It was thus influenced by the lack of seeding particles of adequate size within the core (see Fig. 3a). The particle voids are created by the large centrifugal forces acting on the tracer particles close to the core boundary, leaving only few small tracer particles within the core region. Typical high-speed PIV lasers do not provide sufficient illumination for the detection of these remaining small particles. In combination with a large out-of-plane velocity component of up to $0.25\Omega R = 55$ m/s at the vortex center, this resulted in an inaccurate reconstruction of the 2D3C velocity field within the core. The velocity field was therefore filtered and interpolated prior to the computation of the field operators used for the vortex detection. Ramasamy et al. [12] found

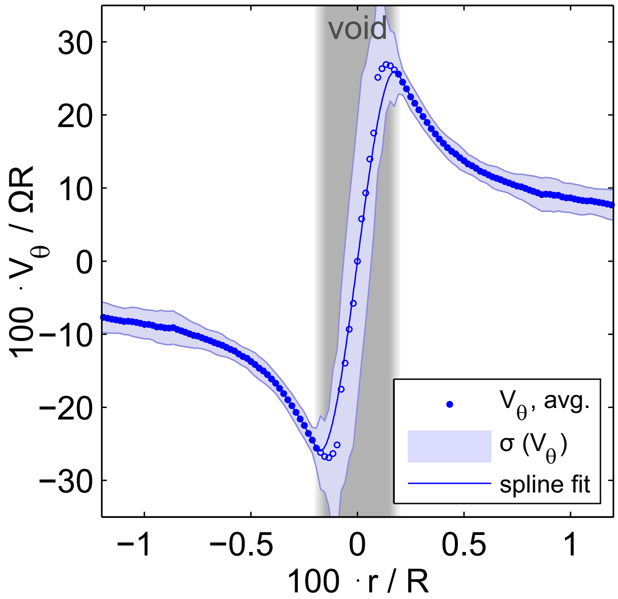

Figure 5: Radial cuts of the instantaneous swirl velocity profile at $\psi_v = 28.87°$ including averaged data points, masked out points within the particle void, and a spline fit

that this filtering had no effect on the center detection for axisymmetric vortices. For asymmetric vortices however, they discovered that only a convolution-based area center method – like the one used in the present study – was able to recover the true vortex center location. The inclination of the vortex axis relative to the measurement plane was determined from BOS measurements to be below $10°$ for the present study. Therefore, no correction of the vortex axis and the velocity components was carried out.

The ratio of the length of the interrogation window L_m and the vortex core radius r_c has to be as small as possible in order to resolve quantitative vortex parameters such as the swirl velocity and the core radius [21]. With the current setup, core radii of between $r_c = 0.02c$ and $r_c = 0.05c$ were measured. Together with a fine interrogation window size of 16×16 pixels, a corresponding measurement resolution of $L_m/r_c = 0.44$ is determined for $r_c = 0.05c$, which compares well with similar rotor blade tip measurements, as listed by van der Wall & Richard [21]. As shown by Richard & van der Wall [14], an overlap of the interrogation windows effectively increases the resolution of PIV. For the present case, this leads to an oversampling resolution of $L_{m,OS}/r_c = 0.11$, well below a critical value of 0.2[4].

Another critical factor for the accurate determination of the swirl velocity is the time delay. The current delay of $\Delta t = 29.4\,\mu s$ corresponds to a blade rotation of $\Delta\Psi = 0.18°$, which is within the range of available results from literature [21]. Martin et al.[11] suggested that the vortex core movement should be restricted to values below 1% of the core radius:

(8) $$\Delta t \frac{\Omega R \lambda_i}{c} < 0.1\%,$$

where λ_i is the non-dimensional inflow velocity and a minimum core radius of $r_c = 5\%c$ is assumed. The time delay in the present test resulted in a value of 0.26%, thus exceeding this criterion. Furthermore, the time delay in combination with the present high out-of-plane velocities near the vortex core led to locally increased out-of-plane loss-of-pairs. An estimated region of $r < 0.5r_c$ exhibited out-of-plane loss-of-pairs for at least one third of the particles.

The vortex positions detected in the present study were influenced by meandering effects due to aperiodic movements of the blades. This in turn was caused by model vibrations, the elasticity of the support, non-uniform blades, and the operation of the rotor in moderate ground effect and recirculation. The vortex positions were therefore determined relative to the blade tip TE positions.

The sample size at each measurement position was restricted to $40-120$ images per vortex age due to high number of test conditions. Although the size of this database still had an influence on the present results, it was found to be large enough to reliably and reproducibly demonstrate the effects of the higher-harmonic control.

Calculating a simple average of meandering vortices produces smoothed out results with diminished maximum swirl velocities. This bias is typically removed by centering the velocity fields on the vortex center positions before computing the mean velocity field, also referred to as *conditional averaging* [24, 9]. For the present data set, the azimuthal location of the maximum swirl velocity varied between individual velocity fields of the same vortex age. This resulted in reduced velocity amplitudes for the conditionally averaged velocity field. Therefore, the values of r_c and V_θ were determined for individual velocity fields and averaged consecutively (see *individual averaging*, [12]).

4 RESULTS & DISCUSSION: BASELINE CASE

At the beginning of each actuation test phase, a baseline (BL) measurement was acquired at nominal test conditions ($T = 2450\,\mathrm{N}$, $\Omega = 109\,\mathrm{rad/s}$). This measurement point serves as a reference for the effects of the active twist actuation and is analyzed in detail within this section.

4.1 Time-resolved vortex tracking

The high image acquisition rate of the PIV setup allowed for the time-resolved capturing of the vortex-induced flow field with azimuthal increments of $\Delta\Psi = 2.81°$. Fig. 6 depicts a sequence of instantaneous velocity fields for vortex ages of $\psi_\mathrm{v} = 3.56° - 45.74°$, corresponding to a total observation time of $6.75\,\mathrm{ms}$ relative to the passing of the quarter chord through the measurement plane at t_0. For reasons of clarity, the relatively long observation time, and the corresponding large azimuthal angle, the measurement planes are assembled parallel to each other rather than with the proper angular offset, and every third velocity plane and fourth vector within the planes are plotted in the graph. The contour plots show the vorticity field normalized with the maximum vorticity $\omega_{z,\mathrm{max}}$ in the center of the vortex at $\psi_\mathrm{v} = 3.56°$. Isosurfaces of the vorticity at discrete levels of $0.15 - 0.6 \cdot \omega_{z,\mathrm{max}}$ are computed between the measurement planes.

The most dominant flow feature in Fig. 6 is the blade tip vortex, which is visualized as a slightly curved dark blue tube that stretches over all measurement planes. The convection of the vortex is clearly visible in the graph and occurs predominantly radially inwards and downwards with the rotor wake. Especially for young vortex ages up to about $\psi_\mathrm{v} = 15°$, the vertical convection rate is close to zero. In addition to the main tip vortex, a sheet of distributed vorticity is created

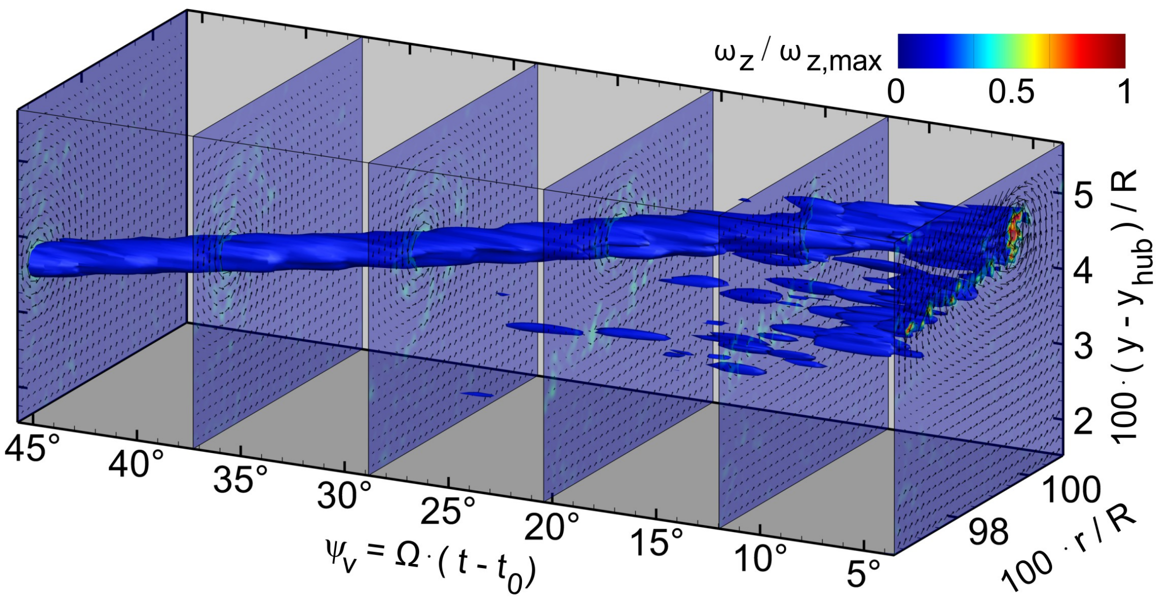

Figure 6: Temporal development of the tip vortex and a vorticity sheet behind the rotor blade at nominal conditions. Only selected vorticity isosurfaces, contour planes, and in-plane velocity vectors are shown for reasons of clarity

in the wake of the passing rotor blade. The vorticity magnitudes that occur within this sheet are small compared to the maximum vorticity in the main vortex core. The outer part of the vortex sheet convects with the swirl velocity field and envelops the vortex core before merging with the tip vortex. The distributed vorticity further away from the tip vortex quickly diffuses, as visible by the disappearance of most of the isosurfaces by a vortex age of about $\psi_v = 15^\circ$. Similarly, the diffusion of the blade tip vortex causes its vorticity magnitude to diminish and its diameter to increase over time. This effect, however, is not visualized by the constant isosurface levels, which leads to the appearance of a shrinking vortex. The maximum swirl velocity V_θ simultaneously decreases. This effect is apparent when comparing the length of the velocity vectors in the first and last cut plane.

Fig. 6 illustrates the quality of data that can be acquired by a PIV system with a high spatial and temporal resolution. Compared to similar 3D vortex visualizations, e.g. presented by Richard & van der Wall [13], Fig. 6 depicts unaveraged data of a single vortex convecting through the measurement domain. Although an even higher temporal resolution would be desirable for the tracking of small-scale vorticity structures – especially in the wake of the blade – the present data set already allows for a detailed analysis of the vorticity field around the tip vortex. Fig. 6 therefore demonstrates possible future applications for the study of blade-vortex interaction effects under simulated forward flight.

4.2 Vortex detection

The detected vortex trajectories of two different measurement runs under nominal conditions and without actuation are plotted in Fig. 7. All 80 individual and time-resolved vortex trajectories are plotted as light blue lines in front of a gray blade contour. The blade contour marks the intersection area between the rotor blades and the PIV measurement plane. The vortex coordinates are given with respect to the detected blade tip trailing edge (TE) positions, which are marked as a red plus and located below the intersection area due to the blade pitch. The average vortex trajectory is given as a dark blue line, the blue dots representing the data points at vortex ages of $\psi_v = 3.56^\circ - 34.49^\circ$. A light blue band of one standard deviation around the average curve is added as a measure of the curve scattering. The general trend of the vortex convection is similar for all individual trajectories with a dominant radial convection towards the rotor mast, which is located to the left of the graph. After their creation at the blade tip, the vortices exhibit a slight upward convection against the direction of the down wash before their direction is reversed. The exact time when this change occurs varies between $\psi_v = 10^\circ - 20^\circ$ for individual trajectories. As previously mentioned, the scattering of the vortex trajectories is a characteristic problem of rotors operated in ground effect and recirculation. The corresponding aperiodicity of the blade movement is shown in the inset of Fig. 7. It depicts a zoomed-in view of the detected individual blade tip TE positions relative to the average position, marked as a red cross. The standard deviation of the vertical tip scattering is of the order of $\pm 0.17\%R$. The horizontal scattering of the blade tip locations results mainly from the inhomogeneous radius of the individual rotor blades and is otherwise negligible. The standard deviation of the uncorrected aperiodicity at the youngest measured vortex age of $\psi_v = 3.56^\circ$ takes on similar values as the tip aperiodicity with $0.19\%R$ in the vertical and $0.07\%R$ in the radial direction. The aperiodicity increases with wake age while the asymmetry of the scattering decreases, resulting in a standard deviation of $0.25\%R$ in the vertical and $0.14\%R$ in the horizontal direction at $\psi_v = 34.49^\circ$.

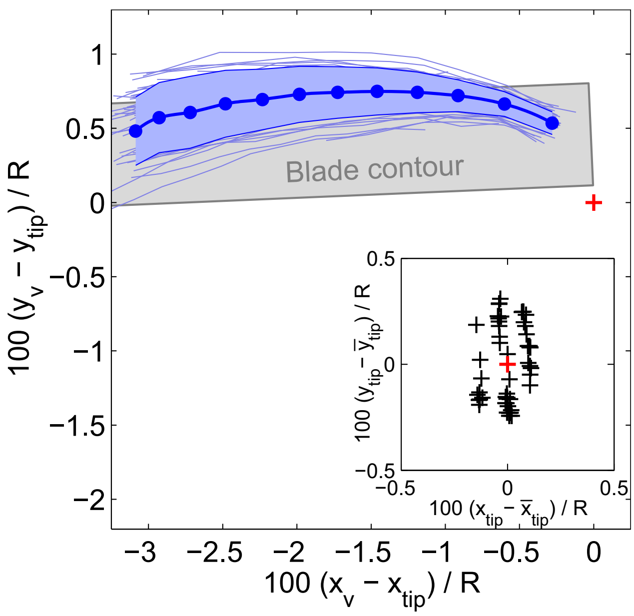

Figure 7: Vortex trajectories of BL case relative to detected blade tip TE position. Inset: scattering of blade tip position

4.3 Vortex characterization

The swirl velocity fields of a sequence of unactuated test runs were determined around the detected vortex positions. Representative trends for the temporal development of the peak swirl and axial velocity components $V_{\theta,z}$ are shown in Fig. 8. The chart depicts the two velocity components normalized by the blade tip speed ΩR and plotted over the vortex or wake age ψ_v. The dots within the chart represent the phase-averaged peak velocity values of 80 individual test sequences. The maximum value for both velocity components is found at the youngest recorded vortex age of $\psi_v = 3.56^\circ$ with $V_{\theta,\mathrm{max}} = 0.35 V_{\mathrm{tip}}$ and $V_{z,\mathrm{max}} = 0.24 V_{\mathrm{tip}}$. Both velocity components decrease substantially by about 18% $V_{\theta,\mathrm{max}}$ and 30% of $V_{z,\mathrm{max}}$ within the first 37.3° of vortex age. This temporal development is approximated by the expression $V_{\theta,z} \propto \psi^{-a}$ with the fit coefficient $a = 0.07$ for V_θ and $a = 0.16$ for V_z. Both fit curves are plotted as solid lines in Fig. 8. The colored bands in Fig. 8 show the standard de-

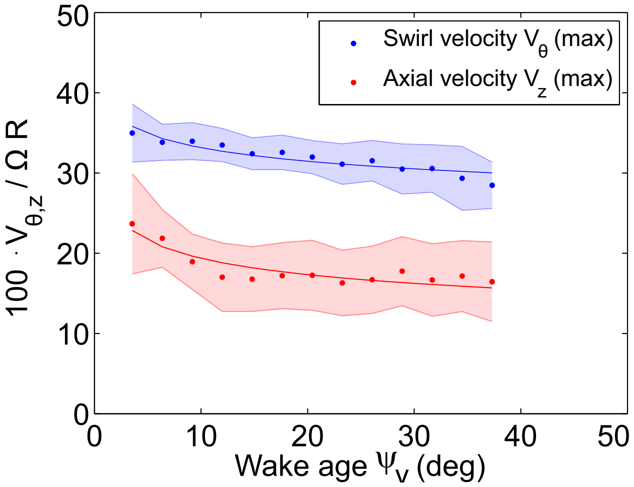

Figure 8: Peak swirl and axial velocities, standard deviations, and simple model fits over vortex age

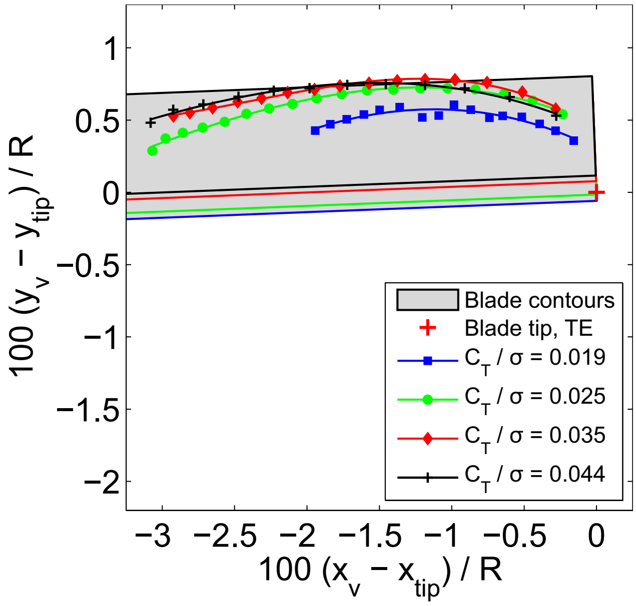

Figure 9: Vortex trajectories for different blade loadings C_T/σ, normalized with the blade tip TE positions

viation around the phase-averaged velocity values, and thus provide a measure for their aperiodicity. For the BL, the standard deviation is of the order of $2.5\% V_{tip}$ for V_θ and $5\% V_{tip}$ for V_z, which illustrates the large cycle-to-cycle variations of the unactuated rotor and the uncertainty in measuring the peak axial component within the particle void.

The present test data is comparable with results from the hover tip structure (HOTIS) test, where a conventional rotor was tested under similar conditions on the same test stand [22]. The initial peak values of the two velocity components compare well with the results from the HOTIS test, but the decrease of the swirl velocity with time is found to be smaller in the present test. The peak axial velocity component shows a clear trend in the present results, while no clear trend is available from the HOTIS data set.

4.4 Thrust variation

In order to determine the Figure of Merit for the BL rotor, a thrust sweep was conducted without active twist actuation. The rotor was operated at a nominal speed of $\Omega = 109\,\text{rad/s}$ with thrust and blade loading settings as specified in Table 1. The corresponding blade tip angles measured with SPR at the $\Psi = 270°$ position are also given in Table 1.

The average vortex trajectories corresponding to blade loadings between $C_T/\sigma = 0.019$ and $C_T/\sigma = 0.045$ are shown in Fig. 9. Consistent with Fig. 7, the vortex trajectories are plotted relative to the blade tip TE positions. The curve corresponding to the highest blade loading of $C_T/\sigma = 0.056$ is not shown in Fig. 9 as the aperiodicity at this thrust setting

Thrust T (N)	1000	1356	1897	2450	3004
Blade loading C_T/σ	0.019	0.025	0.035	0.045	0.056
Tip angle α_{tip} (deg)	3.44	4.24	5.25	6.28	7.23

Table 1: Rotor settings for the thrust sweep

increased by more than a factor of two, which rendered the resulting average curve meaningless. For the other thrust levels, the phase-averaged vortex positions are plotted in the graph, together with fitted polynomial curves as a guide to the eye. Blade contours are plotted in the background of the graph for the shown blade loadings with the corresponding edge colors. The contours represent the intersections between the rotor blades and the PIV measurement plane. The blade tip TE position can therefore be located outside the blade contour. All plotted vortex trajectories feature the same trend of a predominantly radial convection as depicted in Fig. 7. The maximum height of the curves above the TE tip increases with blade loading and stagnates for the nominal thrust case. Simultaneously, the angle of attack and absolute vertical position of the blade tip increase. The trajectories for all blade loadings originate from a position above the TE tip, which suggests that the vortex forms further upstream on the blade. The average convection velocity of the vortex increases with the blade loading from $2.4\% V_{tip}$ at the lowest thrust setting to $5.9\% V_{tip}$ at nominal thrust.

The variation of the initial peak swirl velocity $V_{\theta,max}$ with blade loading is depicted in Fig. 10. The graph contains results from the STAR hover test (red symbols), and data from other rotating- and fixed-wing studies. The present results show a steady increase of the initial peak swirl velocity with blade loading. The swirl velocity for the highest blade loading of $C_T/\sigma = 0.056$, however, does not follow this trend and exhibits a decreased value. As mentioned before, the vortex aperiodicity increased significantly at this measurement point, together with the asymmetry of the young vortices. These influences, in combination with the large particle displacements due to the less than optimal PIV time delay, led to an inability of the PIV system to resolve the high swirl velocity peaks around the vortex.

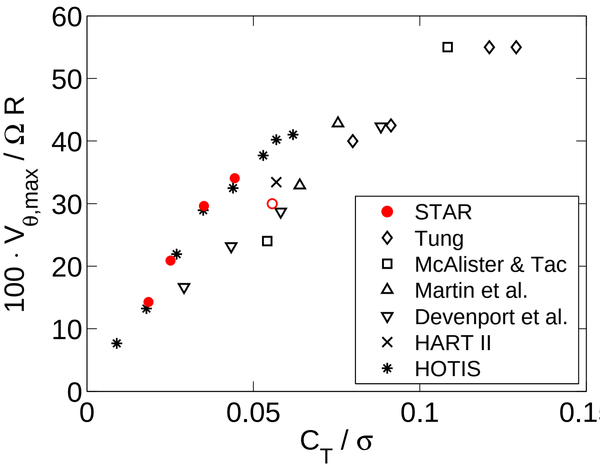

Figure 10: Initial peak swirl velocity over blade loading compared with literature values after [10]

Apart from the outlier at the highest blade loading, the present peak swirl velocity values correlate very well with results from the comparable HOTIS test [22]. The STAR and HOTIS data sets show a steeper rise of the peak swirl velocity over blade loading than the other results from literature. The overall agreement, however, is still acceptable as the scales, blade pre-twists, airfoil shapes, and test conditions vary greatly between these experiments.

5 RESULTS & DISCUSSION: ACTIVE TWIST

The aerodynamic response to a higher-harmonic twist actuation of the STAR rotor is described within this chapter. The present evaluation is based on a series of active twist test cases with $1/rev$ and $3/rev$ actuation frequency and a control amplitude of $U = 600\,$V. The control phase was varied in 45° increments to capture one complete period of the higher-harmonic blade motion. The present analysis is based on the $1/rev$ and $3/rev$ actuation cases as they exhibit the maximum flap and torsion response of the rotor blades, respectively, and therefore the most pronounced effects of the active twist actuation. A preliminary analysis of the PIV data acquired during the STAR hover test was already described in [7]. The earlier analysis, however, was based on instantaneous data and is complemented by a comprehensive data analysis within this paper.

In principle, the higher harmonic control of the blades causes a harmonic change in the elastic torsion and flap bending with a certain phase delay. As the influence of unsteady effects on the blade tip angle is small compared to the effects of elastic torsion, a direct correlation between the blade torsion and blade tip angle can be assumed. The blade tip angle thus oscillates harmonically around the unactuated BL condition. Naturally, the local pitch at the blade tip has a certain influence on the blade aerodynamics. The strength of the blade tip vortices, however, also depends on the exact lift and circulation distribution near the tip, as well as the effective angle of attack of the airfoil relative to the oncoming flow field. Therefore, the vertical blade tip motion caused by the blade flapping also has to be considered, as it induces an additional change of the effective angle of attack. This change amounts to up to 0.7° in amplitude – depending on the actuation frequency – and is proportional to the vertical tip velocity, which runs -90° ahead of the tip oscillation. The resulting effective angle of attack is therefore estimated as a superposition of the BL blade tip angle, the tip torsion angle, and the induced angle due to the vertical tip movement. The flapping and torsion response of the blade occurs with two different and frequency-dependent phase delays.

Hoffmann et al. already discussed the deformation response of the blade tip to the twist actuation in the current measurement campaign [7]. The relevant SPR results for the present evaluation are extracted from this earlier paper and summarized in Fig. 11. The graph depicts the measured changes in the effective angle of attack at the $\Psi = 180^\circ$ blade tip position due to tip torsion and flap-induced blade motion, as affected by harmonic twist actuation with $1/rev$ and $3/rev$ frequency. The markers in the graph indicate the measured data points for the torsion with 45° increments. The thick solid lines represent the mean trend for the tip torsion of all four blades, while the colored bands indicate the corresponding standard deviation. The thick dashed lines represent the flap-induced change of the effective angle of attack.

For the $1/rev$ actuation frequency, the blade deformation measurements show moderate torsion angles of around $|\Delta\alpha_{\text{tip,eff}}| = 1^\circ$ with only slight variation between the four blades. The maximum and minimum blade tip angles are found at actuation phase angles of $\varphi_1 = 160^\circ$ and 340°, respectively. These values were determined for a phase delay in torsion response of about 19°, as measured by the SPR system. The first flap mode of the rotor blades is located at $1.03/rev$, which is close to the $1/rev$ actuation, leading to large blade tip deflections of $17-25\,$mm for the individual

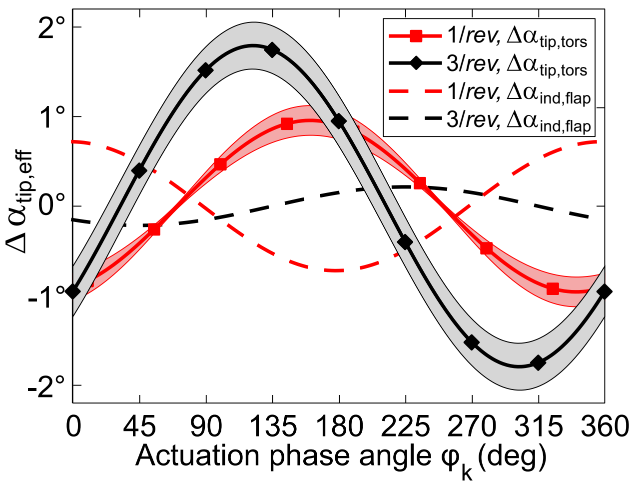

Figure 11: Change in effective blade tip angle over actuation phase angle for k/rev actuation at $\Psi = 180^\circ$ rotor azimuth due to torsion and flap-induced blade motion

blades with a phase delay in flap response of about $92°$. The corresponding maximum vertical velocity of the blade tip is of the order of $2.7\,\mathrm{m/s}$ or $1.2\%V_{\mathrm{tip}}$ and occurs $-90°$ before the peak vertical blade tip deformation. The resulting harmonic change of the effective angle of attack has an amplitude of $|\Delta\alpha_{\mathrm{tip,eff}}| = 0.7°$. The flap-induced change of the effective angle of attack is almost anti-cyclic to the blade tip torsion and effectively counteracts it. The $1/rev$ actuation is therefore expected to have a small effect on the vortex strength and a large effect on the initial vertical location of the vortices.

The blade tip variation in Fig. 11 due to the $3/rev$ blade torsion shows an amplitude of up to $|\Delta\alpha_{\mathrm{tip,eff}}| = 2°$ with peak blade-to-blade variations of $0.5°$ in amplitude and $19°$ in phase delay. The corresponding phase delay in torsion response was quantified as $58°$ by the SPR measurements. The large influence of the harmonic torsion is due to the proximity of the $3/rev$ actuation to the natural torsion frequency of the blades of $3.5/rev$. The maximum and minimum blade tip angles are located around actuation phase angles of $\varphi_3 = 120°$ and $300°$, respectively. The corresponding vertical blade tip deflection of the $3/rev$ active twist is of the order of $5\,\mathrm{mm}$, with a phase delay in flap response of $225°$. The corresponding change of the effective angle of attack is $|\Delta\alpha_{\mathrm{ind,flap}}| = 0.2°$, which therefore causes no significant reduction of the amplitude and only a slight phase shift of the blade tip torsion. The $3/rev$ actuation is therefore expected to have a strong effect on the vortex strength, and a moderate effect on the initial vertical vortex locations.

5.1 Active twist actuation with 1/*rev*

Fig. 12 depicts the impact of the $1/rev$ actuation on the vortex convection. The vortex trajectories are computed as the average of the individual trajectories with respect to the instantaneous blade tip TE positions for Fig. 12a, and with respect to the blade tip TE position of the BL case for Fig. 12b. The BL trajectory is plotted as a black curve and indicates the unactuated reference. The average trajectories of the actuated test cases with different phase angles φ_1 are plotted as colored curves. A blade contour is added in the background of the graph and marks the average intersection area between the rotor blades and the PIV measurement plane. The blade tip TE position is depicted as a red plus sign and located below the blade contour due to the pitch of the blade tip. The actuation phase angle was varied between $\varphi_1 = 10°$ and $325°$ due to a phase offset of $10°$ in the higher harmonic actuation control. The vortex trajectory of the $\varphi_1 = 55°$ case was located above the PIV field of view and is thus not shown in Fig. 12. The trajectories for the phase angles $\varphi_1 = 100°$ and $145°$ were also located close to the upper edge of the PIV field of view and are cut off after a vortex age of about $9.2°$. The other vortex trajectories are visible up to wake ages between $\psi_v = 31.7°$ and $37.3°$. For Fig. 12a, the trajectories exhibit small deviations of less than $0.4\%R$ from the BL trajectory. Only the trajectory corresponding to

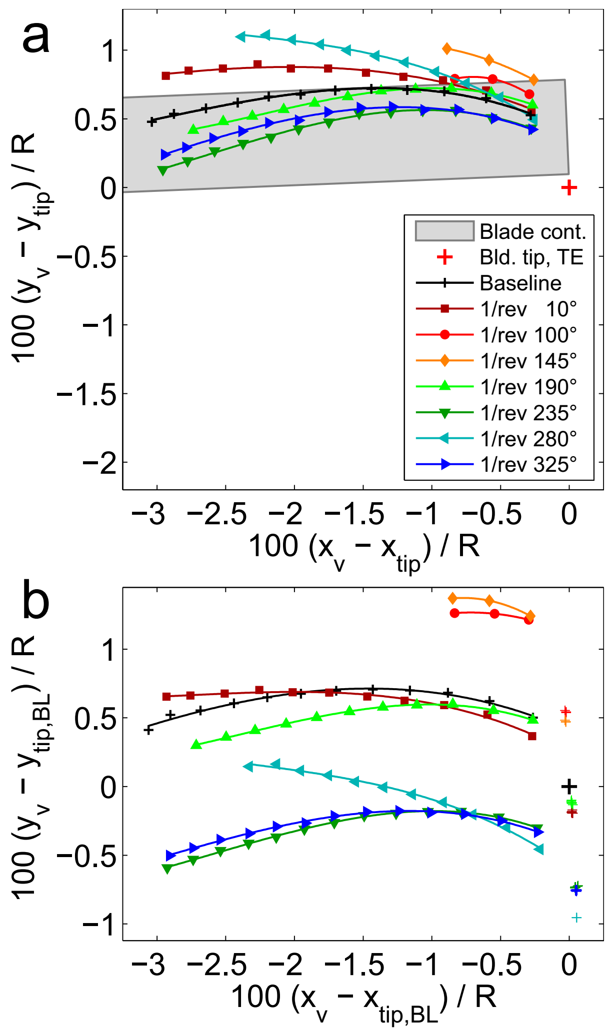

Figure 12: Vortex trajectories for BL case and $1/rev$ actuation with different phase angles φ_1, normalized with a) individual and b) BL blade tip TE positions

a phase angle of $\varphi_1 = 280°$ displays an increased deviation of more than $0.5\%R$, and also the steepest ascent above the tip path plane of all the curves.

Fig. 12b shows the same vortex trajectories as Fig. 12a, but entirely normalized with the blade tip TE position of the BL case. This depiction reveals a strong influence of the $1/rev$ actuation on the vertical blade tip locations, which are plotted as colored plus signs on the right side of the graph. This blade tip displacement also affects the initial vortex positions. The maximum deviations of the vertical blade tip position from the BL case are found for $\varphi_1 = 280°$ with $-0.95\%R$ and for $\varphi_1 = 100°$ with $+0.55\%R$. The initial vortex positions – and therefore the whole vortex trajectories – also show similar levels of displacement. Consequently, the alteration of the young vortex trajectories by the $1/rev$ actuation is dominated by the blade tip deflection and only weakly affected by the variation of the blade tip angle.

The influence of the $1/rev$ active twist actuation on the initial peak swirl velocity $V_{\theta,\mathrm{max}}$ is shown in Fig. 13 for different phase angles φ_1. The maximum swirl velocity of the BL case

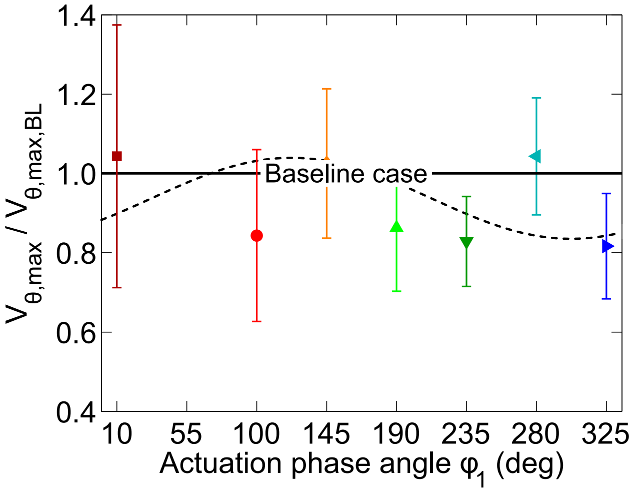

Figure 13: Initial peak swirl velocity relative to BL case for $1/rev$ actuation with different phase angles φ_1. The black dashed curve is a fit proportional to the effective blade tip angle. Other symbols and colors: see legend in Fig. 12a.

without actuation is plotted as a black line. The values of $V_{\theta,\text{max}}$ for the $1/rev$ actuation are plotted over the actuation phase angle φ_1 and relative to the BL case $V_{\theta,\text{max,BL}}$. The standard deviation of the velocity values is indicated by vertical bars. The color and symbols correspond to the plot style in Fig. 12. Again, the value for the phase angle $\varphi_1 = 55^\circ$ is not available, as the corresponding vortices are located outside the PIV field of view. A small mean increase in swirl velocity of $3-5\%$ is noted for the phase angles $\varphi_1 = 10^\circ$, 145°, and 280°. The other phase angles exhibit a decrease in the initial peak swirl velocity of around 16%. The minimum value is found for $\varphi_1 = 325^\circ$ with $V_{\theta,\text{max}} = 0.26\,V_{\text{tip}}$ and an average reduction of 18% compared to the BL value.

The dashed sinusoidal curve in the graph represents the variation of the effective blade tip angle, according to the SPR measurements shown in Fig. 11. Its is used for the comparison of the results with the theoretically predicted vortex strength. The oscillation of the effective angle of attack for the $1/rev$ actuation is found to be small in comparison to the cycle-to-cycle variations of the velocity values. The flap-induced vertical blade tip motion reduces the impact of the active twist actuation on the effective tip angle by up to 65%. For this reason, no clear correlation between the measured and predicted vortex strength over actuation phase angle can be found. This deviation between the predicted and measured vortex strength might also be influenced by the fact that for some actuation phase angles, the formation of the initial vortices was not finished at a vortex age of $\psi_v = 3.56^\circ$. These vortices featured a highly elliptical outline or two smaller vortex cores in the process of merging, resulting in a reduced swirl velocity. This complex relation cannot be described by a simple linear correlation with the blade tip angle and therefore might also explain the deviations. As the excitation of flap motion is much less pronounced for the other actuation frequencies, the $1/rev$ actuation can be regarded as an exceptional test case.

Despite the diminished influence of the higher harmonic $1/rev$ actuation on the vortex strength, a reduction of the peak initial swirl velocity of the tip vortex of up to 18% is detected. The vortex tracking highlights a strong effect of the actuation on the blade tip vortex trajectories. The detected peak vertical blade tip deflection of $-0.95\%R$ correlates well with the SPR measurements. Accordingly, the alteration of the young vortex trajectories by the $1/rev$ actuation is dominated by the blade tip deflection and only weakly affected by the variation of the blade tip angle.

5.2 Active twist actuation with 3/*rev*

The effect of the $3/rev$ actuation on the vortex convection is depicted in Fig. 14, similar to the $1/rev$ actuation in Fig. 12. Again, the vortex trajectories are computed as the average of the individual trajectories with respect to the instantaneous blade tip TE positions for Fig. 14a, and with respect to the blade tip TE position of the BL case for Fig. 14b. The actuated test cases are plotted in color for different phase angles φ_3 and in black for the BL case. The blade intersection with the PIV measurement plane is depicted in the background of Fig. 14a. The blade tip TE position is marked by a red plus sign and located below the blade contour due to the pitch of the blade tip. The trajectory corresponding to the $\varphi_3 = 315^\circ$ case is located above the PIV field of view and therefore not shown in Fig. 14. The other vortex trajectories are visible up to vortex ages between $\psi_v = 34.5^\circ$ and 45.7°. For Fig. 14a, the trajectories corresponding to the phase angles $\varphi_3 = 180^\circ - 360^\circ$ are located close to the BL trajectory and differ from it by less than $0.3\%R$ at the maximum visible vortex age. The vortices corresponding to the phase angles $\varphi_3 = 45^\circ - 135^\circ$ form a second group of trajectories, located below the BL trajectory. The maximum vertical deviation to the BL trajectory occurs for a phase angle of $\varphi_3 = 45^\circ$ and is of the order of $2\%R$.

Fig. 14b shows a second representation of the same vortex trajectories that are plotted in Fig. 14a, but entirely normalized with the blade tip TE position of the BL case. The positions of the blade tip trailing edges corresponding to the actuated test cases are also given with respect to the BL blade tip and marked by colored plus signs. The maximum deviations of the blade tip TE from the BL tip position are of the order of $+0.7\%R$ and $-0.2\%R$, and therefore smaller than for the $1/rev$ case. The reduced blade tip scattering is in accordance with the blade tip deformation measurements presented in [7]. The separation of the vortex trajectories into two groups that is found for the first depiction in Fig. 14a is still present in Fig. 14b. The lower group of trajectories exhibits a behavior similar to the first graph with only slight effects of the blade tip deformation. The basic outline of the upper group of trajectories is also similar to the BL trajectory, but most of the vortex curves within this group are now situated above the BL case due to the considered blade tip deformation.

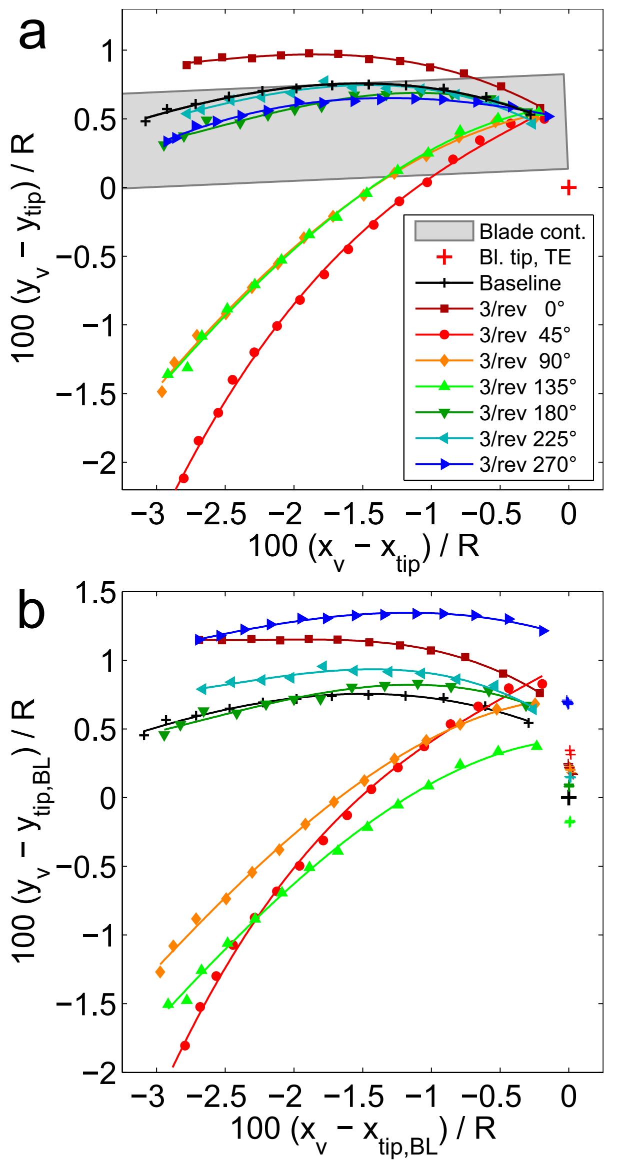

Figure 14: Vortex trajectories for BL case and $3/rev$ actuation with different phase angles φ_3, normalized with a) individual and b) BL blade tip TE positions

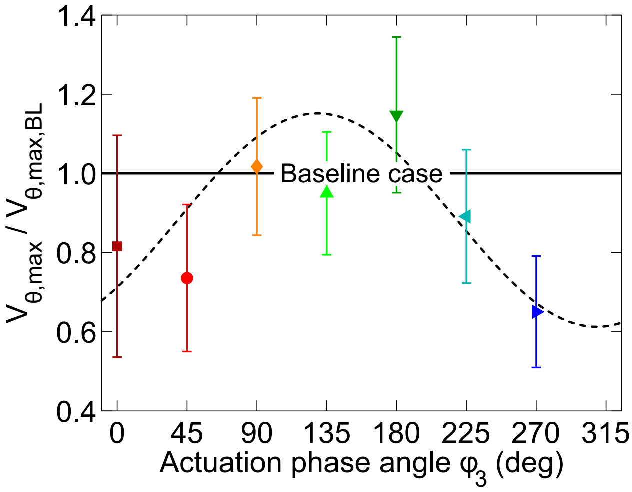

Figure 15: Initial peak swirl velocity relative to BL case for $3/rev$ actuation with different phase angles φ_3. The black dashed curve is a fit proportional to the effective blade tip angle. Other symbols and colors: see legend in Fig. 14a.

Both graphs of Fig. 14 indicate that – for the current $\Psi = 180^\circ$ measurement position – the influence of the active twist actuation with a frequency of $3/rev$ and actuation phase angles in the range of $\varphi_3 = 45^\circ - 135^\circ$ have the highest potential for the variation of the tip vortex path. The $3/rev$ actuation with a phase angle of $\varphi_3 = 45^\circ$ achieves a vertical distance of the vortex to the rotor tip path plane of $2.6\%R$ within the first 45° of wake age. Due to the increasing vertical convection of the vortices with wake age, the miss distance to the following rotor blade – which is a crucial factor for the generation of noise by blade-vortex interactions – is expected to be of the order of $5.5\%R$. The results presented in Fig. 14 demonstrate the effective application of the $3/rev$ active twist actuation for substantially altering the path of the blade tip vortices under hover conditions.

Fig. 15 shows the influence of the $3/rev$ active twist actuation on the initial peak swirl velocity $V_{\theta,\text{max}}$ for different phase angles φ_3 according to the $1/rev$ case presented in Fig 13. The peak value of the BL case without actuation is indicated by a black horizontal line for reference. The initial peak swirl values $V_{\theta,\text{max}}$ are plotted over the actuation phase angle φ_3 and relative to the BL case $V_{\theta,\text{max,BL}}$. The standard deviation of the velocity values is indicated by vertical bars. The actuated test cases are colored according to Fig. 14. Again, the value for the phase angle $\varphi_3 = 315^\circ$ is not available, as the vortices were located outside the PIV field of view.

The $3/rev$ actuation with a phase angle of $\varphi_3 = 180^\circ$ causes an average increase in swirl velocity of about 15% for the youngest vortex age. The values for $\varphi_3 = 90^\circ$ and 135° are located close to the BL case. The other phase angles exhibit a decrease in initial peak swirl velocity of more than 10%. The minimum value is found for $\varphi_3 = 270^\circ$ with $V_{\theta,\text{max}} = 0.2V_{\text{tip}}$ and a reduction of 35% compared to the BL value. This peak reduction in initial vortex strength is about twice as pronounced as for the $1/rev$ actuation, as expected from the excitation of natural blade frequencies (see e.g. Fig. 11).

The dashed curve in Fig. 15 again represents the variation of the effective angle of attack at the blade tip, based on the SPR measurements that were carried out after the PIV measurements. The effective angle of attack is determined via superposition of the active twist torsion at the blade tip with an average phase delay in torsion response of 58°, and the change of the induced angle of attack by the vertical blade tip motion, as effected by the blade flap angle with an average phase delay in flap response of 225°. With the assumption of a linear dependency between the effective blade tip angle and the vortex strength, this would result in a sinusoidal oscillation around the BL value. This, however, does not seem to be the case here, as the measured data exhibits an oscillation around a reduced value of about $0.89\,V_{\theta,\mathrm{max,BL}}$. The curve with the offset correction shows a good correlation with the initial peak swirl velocity variation. Only the peak value around the actuation phase angle of $\varphi_3 = 135°$ exhibits a deviation from the curve, which might have to do with the large time delay of the present PIV setup and the consequent inability to resolve the large flow velocities and gradients likely present for this specific test case.

In summary, the $3/rev$ actuation evokes distinct effects on the strength and paths of the blade tip vortices shed by a hovering rotor. The alteration of the young vortex trajectories is dominated by the harmonic torsion of the blade tip and only weakly affected by the blade tip deflection. Compared to the BL case, the peak swirl velocity is reduced by up to 35% and the vortex trajectories are displaced by up to $2.6\%R$ within the first $45°$ of wake age. Judging by the magnitude of these changes, the active twist actuators are expected to show a similar performance during forward flight, and therefore to constitute an effective measure for the reduction of noise and vibration generated by blade-vortex interactions.

6 CONCLUSIONS

This paper presents results from the hover test of the STAR active twist model rotor. An aerodynamic analysis was conducted based on time-resolved stereoscopic PIV measurements at vortex ages between $\psi_v = 3.56°$ and $45.74°$. This analysis is focused on the effects of the active twist actuation on the trajectories and the strength of the blade tip vortices. The rotor was operated at a nominal speed of $1041\,rpm$, and with a blade loading of $C_T/\sigma = 0.045$. The rotor blades were actuated by integrated piezoceramic twist actuators with actuation frequencies of $1/rev - 5/rev$. Due to actuator endurance issues, the rotor was operated with a reduced active twist control amplitude of 60% of the full control authority. Despite this restriction, a comprehensive test of the actuated rotor was performed under hover conditions with peak torsion amplitudes of up to $2°$.

A three-dimensional representation of the time-resolved flow field behind the blade tip was combined from a series of instantaneous flow fields, including the outline of the vortex and the sheet of vorticity behind the rotor blade. The BL case was further described by its average vortex trajectory, blade tip scattering, and the temporal development of the peak axial and swirl velocity.

Key results from a thrust variation study were presented for a range of blade loadings between $C_T/\sigma = 0.019$ and 0.056. The vortex trajectories for different blade loadings exhibited similarity, except for the convection velocity and maximum height above the tip path plane, which increased with rotor thrust. The initial peak swirl velocity values showed a good overall agreement with other experiments and a very high correlation with results from the HOTIS project.

Active twist actuation cases with $1/rev$ and $3/rev$ actuation frequency were examined to study their effect on the blade tip vortices. These cases were selected as they show the maximum flap and torsion response of the rotor blades, and therefore the most pronounced effects of the active twist actuation. The $1/rev$ actuation achieved a reduction of the initial vortex strength by up to 18% and had a large control authority over the vertical deformation of the blade tips, which peaked at $-0.95\%R$ with respect to the BL case. The alteration of the vortex trajectories by the $1/rev$ actuation was dominated by the blade tip deflection and only weakly affected by the blade tip angle variation.

The $3/rev$ actuation had a strong effect on the initial peak swirl velocity with a peak reduction of up to 35% compared to the BL case. The variation of the swirl velocity over the control phase angle showed a good correlation with the harmonic variation of the effective angle of attack at the blade tip. Actuation with the control phase angles $\varphi_3 = 45° - 135°$ achieved a large variation of the shape of the vortex trajectories with a maximum deviation of $-2.6\%R$ to the rotor tip path plane at a vortex age of $45°$. The alteration of the young vortex trajectories by the $3/rev$ actuation is thus dominated by the torsion of the blade tip and only weakly affected by the blade tip deflection.

The present aerodynamic investigation allowed for a detailed study of the effects of the active twist actuation on the blade tip vortices. The results revealed a high control authority of the actuators – especially for the $3/rev$ actuation frequency – on the shape and vertical offset of the vortex trajectories, and the vortex strength. The outcome of the STAR hover tests, therefore, serves as a proof of functionality of the active twist concept. Judging by the magnitude of the evoked changes, the active twist actuation is expected to constitute an effective measure for the reduction of noise and vibrations generated by blade-vortex interactions.

ACKNOWLEDGEMENT

The technical and financial support of the STAR partners for the test at DLR Braunschweig is highly appreciated. The authors are indebted to R. Keimer and S. Kalow for the development and control of the active twist actuators, the rotor test rig team, especially F. Hoffmann and B. G. van der Wall for the preparation and execution of the hover test, and M. Krebs and K. Kaufmann for technical support.

REFERENCES

[1] R. J. Adrian, K. T. Christensen, and Z.-C. Liu. Analysis and interpretation of instantaneous turbulent velocity fields. *Experiments in Fluids*, 29(3):275–290, 2000.

[2] M. J. Bhagwat and J. G. Leishman. Generalized Viscous Vortex Model for Application to Free-Vortex Wake and Aeroacoustic Calculations. In *Proc. American Helicopter Society 58th Annual Forum*, Montreal, Canada, 2002.

[3] B. Gelhaar, B. Junker, and W. Wagner. DLR Rotor Teststand Measures unsteady Rotor Aerodynamic Data. In *Proc. 19th European Rotorcraft Forum*, Cernobbio, Italy, 1993.

[4] I. Grant. Particle Image Velocimetry: A Review. *Proc. Institution of Mechanical Engineers*, 211 Part C:55–76, 1997.

[5] J. T. Heineck, L. K. Kushner, E. T. Schairer, and L. A. Walker. Retroreflective Background Oriented Schlieren (RBOS) as applied to Full-Scale UH-60 Blade Tip Vortices. In *Proc. American Helicopter Society Aeromechanics Specialists' Conference*, San Francisco, CA, USA, 2010.

[6] F. Hoffmann, S. Opitz, and J. Riemenschneider. Validation of Active Twist Modeling Based on Whirl Tower Tests. In *Proc. American Helicopter Society 65th Annual Forum*, Grapevine, TX, USA., 2009.

[7] F. Hoffmann, O. Schneider, B. G. van der Wall, R. Keimer, S. Kalow, A. Bauknecht, B. Ewers, K. Pengel, and G. Feenstra. STAR Hovering Test - Proof of Functionality and Representative Results. In *Proc. 40th European Rotorcraft Forum*, Southampton, UK, 2014.

[8] J. Jeong and F. Hussain. On the identification of a vortex. *Journal of Visalization*, 285:69–94, 1995.

[9] J. G. Leishman. Measurements of the aperiodic wake of a hovering rotor. *Experiments in Fluids*, 25(4):352–361, 1998.

[10] P. B. Martin and J. G. Leishman. Trailing vortex measurements in the wake of a hovering rotor blade with various tip shapes. In *Proc. American Helicopter Society 58th Annual Forum*, pp. 1–23, Montreal, Canada, 2002.

[11] P. B. Martin, J. G. Leishman, G. J. Pugliese, and S. L. Anderson. Stereoscopic PIV Measurements in the Wake of a Hovering Rotor. In *Proc. American Helicopter Society 56th Annual Forum*, pp. 1–19, Virginia Beach, VA, USA, 2000.

[12] M. Ramasamy, R. Paetzel, and M. J. Bhagwat. Aperiodicity correction for rotor tip vortex measurements. In *Proc. American Helicopter Society 67th Annual Forum*, Virginia Beach, VA, USA, May 2011.

[13] H. Richard, J. Bosbach, A. Henning, M. Raffel, and B. G. van der Wall. 2C and 3C PIV measurements on a rotor in hover condition. In *Proc. 13th International Symposium on Applications of Laser Techniques to Fluid Mechanics*, Lisbon, Portugal, June 2006.

[14] H. Richard and B. van der Wall. Detailed investigation of rotor blade tip vortex in hover condition by 2C and 3C-PIV. In *Proc. 32nd European Rotorcraft Forum*, Maastricht, the Netherlands, 2006.

[15] J. Riemenschneider, R. Keimer, and S. Kalow. Experimental Bench Testing of an Active-Twist Rotor. In *Proc. 39th European Rotorcraft Forum*, Moscow, Russia, 2013.

[16] J. Riemenschneider, P. Wierach, S. Opitz, and F. Hoffmann. Testing and simulation of an active twist rotor blade. In *Proc. Adaptronic Congress*, Göttingen, Germany, 2007.

[17] D. Roth, B. Enenkl, and O. Dieterich. Active Rotor Control by Flaps for Vibration Reduction - Full scale demonstrator and first flight test results -. In *Proc. 32nd European Rotorcraft Forum*, Maastricht, the Netherlands, 2006.

[18] V. Roussinova and R. Balachandar. *River Flow*. CRC Press, Boca Raton, FL, USA, 2012.

[19] W. R. Splettstoesser, R. Kube, W. Wagner, U. Seelhorst, A. Boutier, F. Micheli, E. Mercker, and K. Pengel. Key results from a higher harmonic control aeroacoustic rotor test (HART). *Journal of the American Helicopter Society*, 42(1):58–78, 1997.

[20] B. G. van der Wall, C. L. Burley, Y. H. Yu, K. Pengel, and P. Beaumier. The HART II Test - Measurement of Helicopter Rotor Wakes. *Aerospace Science and Technology*, 8(4), 2004.

[21] B. G. van der Wall and H. Richard. Analysis methodology for 3C-PIV data of rotary wing vortices. *Experiments in Fluids*, 40:798–812, 2006.

[22] B. G. van der Wall and H. Richard. Hover Tip Vortex Structure Test (HOTIS) - Test Documentation and Representative Results. Technical report, DLR, Brunswick, Germany, 2008.

[23] G. H. Vatistas, V. Kozel, and W. C. Mih. A simpler model for concentrated vortices. *Experiments in Fluids*, 11(1):73–76, 1991.

[24] A. Vogt, P. Baumann, J. Kompenhans, and M. Gharib. Investigations of a wing tip vortex in air by means of DPIV. *Advanced Measurement and Ground Testing Conference*, 1996.

[25] P. Wierach, J. Riemenschneider, S. Optiz, and F. Hoffmann. Experimental investigation of an active twist model rotor blade under centrifugal loads. In *Proc. 33rd European Rotorcraft Forum*, Kazan, Russia, 2007.

[26] M. L. Wilbur, W. T. J. Yeager, W. K. Wilkie, C. E. S. Cesnik, and S. J. Shin. Hover Testing of the NASA/ARMY/MIT Active Twist Prototype Blade. In *Proc. American Helicopter Society 56th Annual Forum*, pp. 1–14, Virginia Beach, VA, USA, 2000.

[27] J. Zhou, R. J. Adrian, S. Balachandar, and T. M. Kendall. Mechanisms for generating coherent packets of hairpin vortices in channel flow. *Journal of Fluid Mechanics*, 387:353–396, 1999.